AGU PUBLICATIONS

Water Resources Research

RESEARCH ARTICLE
10.1002/2016WR018934

This article is a companion to *Li et al.* [2017], doi:10.1002/2016WR018935.

Special Section:
Concentration-discharge Relations in the Critical Zone

Key Points:
- We developed RT-Flux-PIHM to integrate land-surface interactions, hydrology, and reactive transport processes at the watershed scale
- RT-Flux-PIHM offers capabilities to integrate data and understand processes across hydrology and geochemistry
- Watershed topography dictates spatial distribution of water content and dissolution rates; ion exchange leads to CQ hysteresis loops

Correspondence to:
L. Li,
lili@engr.psu.edu

Citation:
Bao, C., L. Li, Y. Shi, and C. Duffy (2017), Understanding watershed hydrogeochemistry: 1. Development of RT-Flux-PIHM, *Water Resour. Res.*, *53*, doi:10.1002/2016WR018934.

Received 14 MAR 2016
Accepted 8 FEB 2017
Accepted article online 15 FEB 2017

Understanding watershed hydrogeochemistry: 1. Development of RT-Flux-PIHM

Chen Bao[1], Li Li[2], Yuning Shi[3], and Christopher Duffy[2]

[1]John and Willie Leone Department of Energy and Mineral Engineering, Pennsylvania State University, University Park, Pennsylvania, USA, [2]Department of Civil and Environmental Engineering, Pennsylvania State University, University Park, Pennsylvania, USA, [3]Department of Ecosystem Science and Management, Pennsylvania State University, University Park, Pennsylvania, USA

Abstract Model development in hydrology and geochemistry has been advancing separately with limited integration. We developed a watershed hydrogeochemical code RT-Flux-PIHM to understand complex interactions between hydrological processes (PIHM), land-surface processes (FLUX—Noah Land Surface Model), and multicomponent subsurface reactive transport (RT). The RT module simulates geochemical processes including aqueous complexation, surface complexation, mineral dissolution and precipitation, and cation exchange. The RT module is verified against the widely used reactive transport code CrunchFlow. The code uses semidiscrete finite volume method and irregular gridding and offers data harvesting capabilities from national databases. The application of RT-Flux-PIHM is demonstrated in the Susquehanna Shale Hills Critical Zone Observatory (SSHCZO). We aim to understand key processes that govern hydrogeochemical dynamics of the nonreactive chloride and reactive magnesium. Simulation results indicate that watershed characteristics, in particular topography, dictate the spatial distributions of water content and soil dissolution rates. Ion exchange provides buffering capacities and leads to a hysteresis loop of concentration and discharge relationship of magnesium, which differs from the open hysteresis of chloride. RT-Flux-PIHM offers physics-based modeling capabilities to integrate the vast amount of water and chemistry data that have now become available, to differentiate the relative importance of competing processes, and to test hypotheses at the interface of hydrology and geochemistry.

1. Introduction

Hydrological and geochemical process dynamics at the watershed scale are complex. Land-surface processes partition energy while surface hydrological processes partition rainwater into atmosphere, plants, surface water, and subsurface reservoirs (soil and aquifer) [*Brooks et al*., 2015; *Montanari et al*., 2015]. Water drives abiotic reactions including mineral dissolution and precipitation, surface and aqueous complexation, as well as biotic reactions such as soil carbon and nutrient decomposition. The interactions between hydrological and geochemical processes modify water chemistry, and therefore have profound impacts on water quality [*Craig et al*., 2010; *Kirchner and Neal*, 2013], chemical weathering [*Gaillardet et al*., 1999; *Navarre-Sitchler and Brantley*, 2007; *White*, 1995], and biogeochemical cycling [*Boyer et al*., 1997; *Kump et al*., 2000]. Understanding complex interactions between water, energy, and fluxes at the watershed scale requires an integrated framework across disciplinary boundaries of hydrology and geochemistry [*Duffy et al*., 2014].

Existing studies and model developments however are often fragmented within distinct disciplinary boundaries. In the geochemistry community, multicomponent Reactive Transport Models (RTMs) originated in the 1980s [*Chapman*, 1982; *Chapman et al*., 1982]. RTMs integrate flow and solute transport and biogeochemical reactions including mineral dissolution and precipitation, ion exchange, surface complexation, as well as microbe-mediated redox reactions, biomass growth and decay. RTMs solve partial differential equations coupling flow and transport within a full geochemical thermodynamic and kinetic framework [*Steefel et al*., 2015], therefore enabling explicit tracing of spatial and temporal evolution of multiple geochemical species in fluid and solid phases [*Li et al*., 2017a]. Built upon the theoretical and computational foundation of reaction thermodynamics and kinetics [*Helgeson et al*., 1984a; *Lasaga*, 1981; *Lichtner*, 1985, 1988], RTM development took gigantic strides in the 1990s showcasing the extensive use of RTM codes in the past decades [*Bethke*, 1996; *Hammond et al*., 2014; *Lichtner et al*., 1996; *Mayer et al*., 2002; *Ortoleva et al*., 1987; *Steefel and*

Lasaga, 1994; *Van Cappellen and Wang*, 1996; *White and Oostrom*, 2000; *Xu et al.*, 1999; *Yeh and Tripathi*, 1989].

RTMs have been utilized as integration and interpretation tools in a diverse array of subsurface environments involving porous and fractured media [*Li et al.*, 2017b; *MacQuarrie and Mayer*, 2005; *Steefel et al.*, 2005; *Prommer et al.*, 2003]. RTMs have been applied to understand processes relevant to chemical weathering [*Bolton et al.*, 1996; *Brantley and Lebedeva*, 2011; *Maher et al.*, 2009; *Moore et al.*, 2012], biogeochemical cycling in marine sediments [*Dale et al.*, 2008; *Krumins et al.*, 2013; *Regnier et al.*, 1997], environmentally bioremediation [*Druhan et al.*, 2012; *Li et al.*, 2010], natural attenuation [*Liu et al.*, 2008; *Mayer et al.*, 2001], geological carbon sequestration [*Brunet et al.*, 2016; *Navarre-Sitchler et al.*, 2013; *Xu et al.*, 2003; *Zhang et al.*, 2013], nuclear waste storage [*Saunders and Toran*, 1995; *Soler and Mader*, 2005], and energy production [*Audigane et al.*, 2007; *Qiao et al.*, 2015]. RTM studies have so far mostly been applied at the spatial scales of pores at microns [*Fang et al.*, 2011; *Kang et al.*, 2006; *Li et al.*, 2006, 2008; *Molins et al.*, 2014; *Scheibe et al.*, 2015], to columns at tens of centimeters [*Liu et al.*, 2013; *Salehikhoo and Li*, 2015], and to field scales at tens of meters with the capability of explicitly taking into account subsurface spatial heterogeneity [*Bao et al.*, 2014; *Yabusaki et al.*, 2011]. Only until recently have subsurface reactive transport processes started to be simulated at the watershed scale and beyond [*Beaulieu et al.*, 2011; *Beisman et al.*, 2015; *Navarre-Sitchler et al.*, 2013; *Yeh et al.*, 2006]. Regional scale RTMs have been linked to global vegetation models to understand the role of climate change in controlling weathering over periods of 10° to 10^{3} years [*Godderis et al.*, 2006; *Goddéris et al.*, 2013; *Roelandt et al.*, 2010].

The hydrology community, on the other hand, has utilized distributed models for about five decades to understand hydrological processes including precipitation, infiltration, runoff, surface and subsurface water

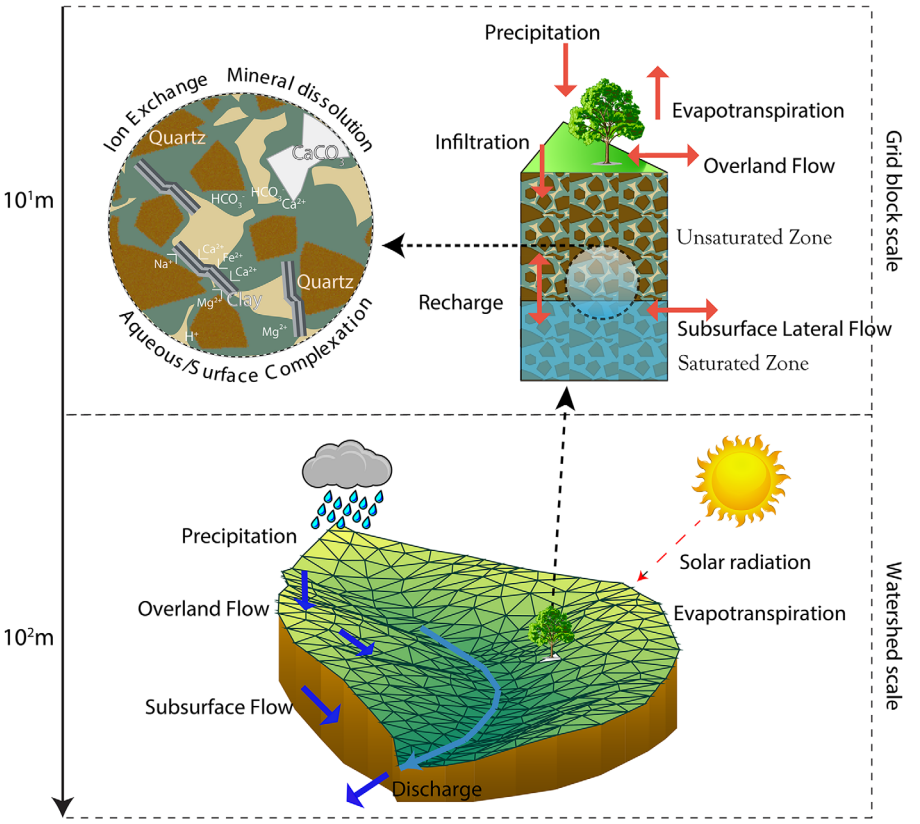

Figure 1. A schematic representation of processes in RT-Flux-PIHM. Flux-PIHM simulates the hydrological and land-surface dynamics (precipitation, canopy interception, infiltration, recharge, overland flow, subsurface lateral flow, river flow, and surface energy balance) at the watershed scale using the semidiscrete finite volume method. The RT module takes the water output from Flux-PIHM and simulates multicomponent reactive transport processes for the spatiotemporal evolution of chemical species in the water phase. The discretized mesh structure for the Susquehanna Shale Hills Critical Zone Observatory (SSHCZO) is depicted here. Geochemical processes in the RT module include mineral dissolution and precipitation, ion exchange, surface complexation, aqueous complexation, among others.

interactions, snow melting, and river hydrodynamics in a spatially explicit manner [*Abbott et al*., 1979; *Beven*, 1989; *Freeze and Harlan*, 1969; *Gan et al*., 2006; *James*, 1972; *Jarboe and Haan*, 1974; *Kumar et al*., 2009; *McDonnell et al*., 2007; *Qu and Duffy*, 2007; *Quinn et al*., 1991; *Refsgaard and Storm*, 1995; *Shen and Phanikumar*, 2010; *Therrien et al*., 2010; *VanderKwaak and Loague*, 2001]. The recent introduction of land-surface processes into hydrological models marks a new advance toward more accurate representation of surface energy balance [*Maxwell and Miller*, 2005; *Shi et al*., 2013]. Solute and water quality models have been developed as add-on modules to hydrological models to understand environmental impacts of contaminants [*Arnold et al*., 1998; *Donigian et al*., 1995; *Santhi et al*., 2001]. These modules however often use empirical and simplified relationships and do not incorporate physics-based multicomponent reaction networks and rigorous thermodynamics and kinetics representations [*Davison et al*., 2014].

Although model development within distinct disciplines has advanced significantly, limited integration across hydrology and geochemistry has impeded our ability to understand and predict watershed hydrogeochemical processes and to address relevant environmental problems [*Grimm et al*., 2003]. For example, efforts of understanding watershed hydrogeochemical dynamics date back to more than half a century ago in understanding stream chemistry (Cl) from the Hubbard Brook forest in New Hampshire [*Johnson et al*., 1969]. More than three decades later, we are still grappling with the hydrogeochemical Double Paradox of rapidly mobilized old water with highly variable responses in stream chemistry under changing hydrological conditions [*Bishop et al*., 2004; *Godsey et al*., 2009; *Kirchner*, 2003]. Here we develop a multicomponent reactive transport module (RT) to integrate into Flux-PIHM [*Shi et al*., 2013], the distributed hydrologic model Penn State Integrated Hydrological Model (PIHM) [*Qu and Duffy*, 2007] with a land-surface module adapted from the Noah Land Surface Model (LSM) (Figure 1). RT-Flux-PIHM offers capabilities to integrate data, process, and system complexities, to elucidate controls of watershed dynamics, as well as to carry out virtual experiments for projection into the future. This paper primarily focuses on model development; a companion paper focuses on the application of the model in Susquehanna Shale Hills Critical Zone Observatory to understand concentration-discharge relationships [*Li et al*., 2017].

2. RT-Flux-PIHM

2.1. Model Structure Overview

RT-Flux-PIHM contains three modules: the Noah LSM, PIHM, and RT (Figure 2). The Flux-PIHM modules were developed in previous work [*Shi et al*., 2013]; the new addition in this work is the multicomponent reactive transport module RT. The Noah LSM is the land-surface module that solves surface energy balance [*Chen and Dudhia*, 2001; *Shi et al*., 2013]. It simulates surface heat fluxes (sensible, latent, and ground heat fluxes), canopy water balance, internal soil heat and moisture fluxes, and snow processes. When coupled with PIHM, the model output of net precipitation, soil evaporation, and transpiration from Noah LSM feed into PIHM for the calculation of surface and groundwater interactions (surface runoff, infiltration, recharge, subsurface lateral flow, channel routing) (Figure 1). The RT module uses calculated water distribution and flow rates from Flux-PIHM and solves advection dispersion reaction (ADR) equations for the spatiotemporal

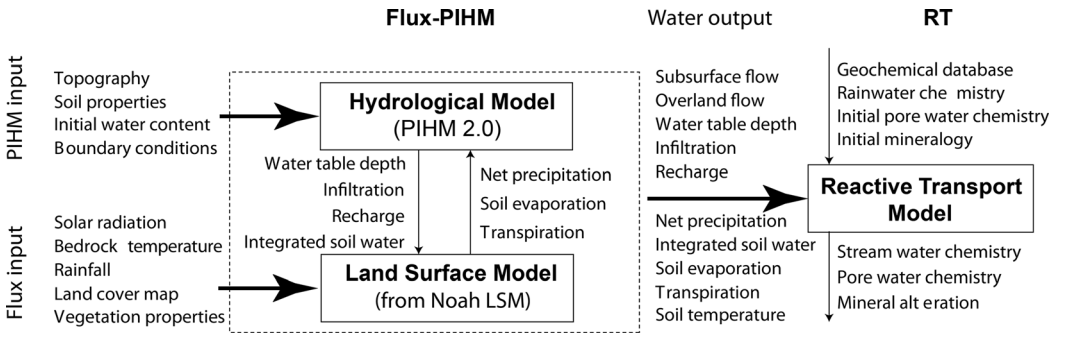

Figure 2. A schematic representation of input, output, and process coupling in RT-Flux-PIHM. The Flux-PIHM module solves the hydrological and land-surface dynamics and is two-way coupled. The RT module reads flow and water distribution calculated from Flux-PIHM specifies initial and boundary chemistry of water and solid phases and calculates the spatiotemporal evolution of aqueous and solid phase composition based on hydrological conditions and geochemical thermodynamics and kinetics.

evolution of aqueous and solid phase composition. The RT module is therefore driven by the water calculation in Flux-PIHM. Alterations in aqueous and mineralogical composition are assumed to have negligible impacts on hydrological processes at the time scale of months to years. The RT module can be run after the entire Flux-PIHM simulation is finished. It can also be run after specified time steps of Flux-PIHM. The first mode is computationally more efficient. The second mode would facilitate calibration of the integrated model to both physical and geochemical observations.

The connection between the three modules is the water content. As discussed in *Shi et al*. [2013], the ability of simulating surface energy balance in PIHM improves the prediction of water fluxes, including evapotranspiration, total runoff (discharge), and peak discharge events especially after extended dry periods. Model results from Flux-PIHM reveal that the position of water table, especially near the stream, is strongly correlated to average sensible and latent heat fluxes. These insights cannot be obtained through PIHM or Noah LSM alone. Accurate estimation for water fluxes and content is also important in simulating geochemical processes, the driver of which is often the infiltration of fresh rainwater at disequilibrium with soil minerals, as will be discussed later.

The coupling strategy maintains mass balance in surface and subsurface processes for water and chemical species. Momentum is conserved in subsurface processes where Darcy's law or Richards equation governs flow dynamics. In surface hydrological processes, momentum is not strictly conserved [*Qu and Duffy*, 2007]. Energy balance is achieved in the soil up to 200 cm deep by considering the vertical heat conduction within each prismatic element. RT-Flux-PIHM discretizes the simulation domain into unstructured prismatic elements, which allows accurate and flexible representation of watershed topography and boundaries. Detailed processes and equations of Flux-PIHM are in literature [*Qu and Duffy*, 2007; *Shi et al*., 2013]. Here we briefly discuss governing equations in RT-Flux-PIHM.

2.2. The Noah Land-Surface Module

The Noah LSM in Flux-PIHM has undergone extensive testing and has been implemented into mesoscale atmospheric models [*Boone et al*., 2004; *Ek et al*., 2003; *Xia et al*., 2012]. It captures diel and seasonal variations in surface heat fluxes and land-surface temperature with relatively few parameters. The Noah LSM solves water content and temperature of one canopy layer and several soil layers. The volumetric soil moisture equations in the Noah LSM are adapted to allow coupling with PIHM. The soil water retention model, the canopy water capacity formulation, and the canopy drip rate formulation in the Noah LSM are replaced by the PIHM formulations in the coupled land-surface scheme. Here we focus on presenting governing equations for soil temperature and moisture that are more relevant to RT. Details of the coupling between the Noah LSM and PIHM are in literature [*Shi et al*., 2013].

The prismatic volume of each PIHM grid is divided into four soil layers depending on the depth of the prism. From the ground surface to the lower boundary of the subsurface ("bedrock"), the standard thicknesses of the top four soil layers are 0.1, 0.3, 0.6, and 1.0 m, respectively, as in the Noah LSM. If the bedrock depth is less than 2 m, the number of soil layers and the thickness of the lowest layer are adapted to match the depth of bedrock. If the bedrock depth is larger than 2 m, additional soil thickness is added as needed to the bottom of the soil layer.

The Noah LSM solves the soil temperature at the four soil layers in each prismatic finite volume:

$$C(\Theta)\frac{\partial T_s}{\partial t}=\frac{\partial}{\partial z}\left[K_t(\Theta)\frac{\partial T_s}{\partial z}\right], \tag{1}$$

where Θ is the volumetric soil water content (volume of soil water per volume of soil) ($m^3\ m^{-3}$), T_s is the soil temperature (K), and z is the depth of soil (m). The volumetric heat capacity C (J m^{-3} K^{-1}) and thermal conductivity K_t (W m^{-1} K^{-1}) are functions of soil water content and the heat capacity of water, soil, and air.

The Richards equation calculates the volumetric soil water content in different layers. The soil layers below the water table are set to be saturated, thus only the layers above the water table are calculated. The groundwater recharge rate is calculated in PIHM. For the soil water content in the top soil layer, we have

$$d_{z_1}\frac{\partial\Theta_1}{\partial t}=-D_1\left(\frac{\partial\Theta}{\partial z}\right)_{z_1}-K_{z_1}+I-E_{soil}-E_{t1}; \tag{2a}$$

for the bottom soil layer J above the water table,

$$d_{z_J}\frac{\partial\Theta_J}{\partial t}=D_J\left(\frac{\partial\Theta}{\partial z}\right)_{z_{J-1}}+K_{z_{J-1}}-R-E_{tJ}; \tag{2b}$$

and for the layer j in between,

$$d_{z_j}\frac{\partial\Theta_j}{\partial t}=D_{j-1}\left(\frac{\partial\Theta}{\partial z}\right)_{z_{j-1}}-D_j\left(\frac{\partial\Theta}{\partial z}\right)_{z_j}+K_{z_{j-1}}-K_{z_j}-E_{tj}; \tag{2c}$$

where d_{zj} is the thickness of the jth soil layer; K ($=K\times dz/dz$) is the hydraulic conductivity; D is the soil water diffusivity; E_{soil} is the soil evaporation; E_{tj} represents the canopy transpiration by roots in the jth layer; I is the infiltration; and R is the groundwater recharge. Both I and R are calculated in PIHM, which provide more realistic estimation than the original LSM. On the other hand, the Noah LSM evapotranspiration formulation provides more realistic calculation of transpiration from the rooting zone (E_{tj}).

2.3. The Hydrological Module PIHM

PIHM solves for five unknowns that describe water storage (m^3/m^2) in each prismatic element: aboveground storage in vegetation canopy, snow, and ground surface (water on land surface that forms overland flow), and belowground storage in unsaturated and saturated zones [*Zhang et al*., 2016]. Each storage volume is normalized by the base land-surface area of the prismatic element. The total depth of the subsurface is from the ground surface (upper subsurface boundary) to the impermeable bedrock (lower subsurface boundary). The depths of unsaturated and saturated zones are not prescribed and are calculated during the simulation. PIHM is essentially a 2.5-D model with full discretization in the x and y directions and coarse discretization in the z direction with ground surface, unsaturated, and saturated zones. Layered subsurface structure has been added to other modules of PIHM [*Kumar et al*., 2009].

As discussed in PIHM papers [*Qu and Duffy*, 2007; *Zhang et al*., 2016], the semidiscrete finite volume method is applied to the partial differential forms of governing equations by integrating the equations over a three-dimensional control volume, thereby converting them to ordinary differential equations (ODEs) of individual prismatic elements. The local systems of ODEs are assembled to form a global ODE system, which is then solved by an ODE implicit solver. Here we present the semidiscrete form of the equations for water storage above ground, unsaturated zone, and saturated zone. The land-area normalized surface water storage in element i depends on flow rates in and out of the element (all with subscript i) in the following semidiscrete form:

$$\frac{dh_{s,i}}{dt}=p_{net,i}-I_i-E_{soil,i}-\sum_{j=1,N_{i,1}}^{N_{i,3}}q_{s,ij}, \tag{3}$$

where h_s is the water storage above the land surface. The rates of net precipitation, i.e., precipitation not intercepted by canopy (p_{net}), infiltration from land surface to unsaturated zone (I), evaporation from soil (E_{soil}), and lateral surface flow from element i to j ($q_{s,ij}$) are all normalized by the base area of the finite volume [$m^3/(m^2\ s)$]. $N_{i,1\sim3}$ is the index of the neighboring elements of i. The flux rates p_{net} and E_{soil} are computed in the land-surface module (Noah LSM) while $q_{s,ij}$ is calculated based on a diffusion wave approximation of the 2-D St. Venant equation [*Gottardi and Venutelli*, 1993]. The surface water determines the amount of overland flow.

Land-area normalized water storages in the unsaturated and saturated zones of element i are calculated as follows:

$$\theta\frac{dh_{u,i}}{dt}=I_i-R_i-E_{soil,i}-E_{t,i}, \tag{4}$$

$$\theta \frac{dh_{g,i}}{dt} = R_i - q_{bedrock,i} - \sum_{j=N_{i,1}}^{N_{i,3}} q_{g,ij}, \quad (5)$$

where h_u and h_g are the water storages in the unsaturated and saturated zones (ground water), respectively; θ is the porosity (m^3 pore space/m^3 porous medium); R is the recharge rate from unsaturated zone into the saturated zone; E_t is the canopy transpiration from unsaturated zone; $q_{bedrock}$ is downward flow rate into bedrock [$m^3/(m^2\ s)$]; $q_{g,ij}$ is lateral flow rate [$m^3/(m^2\ s)$] from element i to j in the saturated zone, which is calculated using Darcy's law. The soil evaporation term E_{soil} is subtracted from surface water if surface water is present (equation (3)). Otherwise, it will be taken from the unsaturated zone.

Flux-PIHM assumes a zero flux boundary condition at the bedrock. By doing so, the model is most suitable for calculating shallow soil water that directly interacts with the surface water. Additional deeper groundwater layer however can be added for deeper aquifers by assuming nonzero q_{bedrock} in equation (5). Recharge and infiltration are calculated based on steady state Richards equation [*Duffy*, 2004]. An integration over the unsaturated zone using the van Genuchten type soil retention characteristic is used to simplify the calculation of recharge and infiltration [*Qu and Duffy*, 2007; *Van Genuchten*, 1980]. Macropores (vertical and horizontal) are represented from the land surface to a predefined macropore depth [*Beven and Germann*, 1982; *Shi et al*., 2013].

In the unsaturated zone, lateral flow rates are assumed to be zero and only vertical flow occurs, a common assumption for the unsaturated zone [*Zhu et al*., 2012]. The division between the unsaturated and saturated zones represents hydrological dynamics in the soil layer where water is sufficient to form lateral flow into the stream. Within each element, the saturated and unsaturated zones are divided by the water table. Because the position of the water table varies in time and space, so are the thicknesses of the saturated and unsaturated zones. Note that this shallow groundwater flow in soil zone is called "groundwater" in PIHM literature [*Duffy et al*., 2009; *Kumar et al*., 2009; *Li and Duffy*, 2012; *Qu and Duffy*, 2007]. It is however different from the regional groundwater reservoirs in the deeper subsurface.

2.4. The Reactive Transport Module RT

Reactive transport equations. Reactive transport codes solve mass conservation equations for chemical species that are involved in chemical and biological reactions in the subsurface [*Steefel et al*., 2014]. Chemical reactions include equilibrium-controlled and kinetic-controlled reactions. Equilibrium-controlled fast reactions include aqueous complexation, ion exchange and surface complexation, while kinetic-controlled reactions typically include mineral dissolution and precipitation and redox reactions. This leads to the partition into primary (basis) species that are the building blocks of chemical systems and secondary species whose concentrations can be calculated from concentrations of primary species using laws of mass action for equilibrium-controlled reactions [*Lichtner*, 1985]. The RT module considers advective, dispersive/diffusive transport, and geochemical reactions using the finite volume method [*Xu et al*., 2006].

Following the classic reactive transport formulation, the RT module considers advective, dispersive/diffusive transport, and geochemical reactions using the finite volume method [*Xu et al*., 2006]. The advection dispersion reaction (ADR) equations are written for primary species (basis set) [*Lichtner*, 1996; *Steefel and Lasaga*, 1994; *Yeh and Tripathi*, 1989]. An example partial differential equation (PDE) is shown here for one of the primary species m:

$$\frac{\partial (S_w \theta C_m)}{\partial t} = \nabla \cdot (\mathbf{D} \nabla C_m - \mathbf{u} C_m) + r_m + ss_m, \qquad m = 1, np \quad (6)$$

where S_w is the water saturation (m^3 water/m^3 pore space); C_m is the aqueous concentration of m (mol/m^3 water); $\mathbf{D}$ is the dispersion/diffusion tensor (m^2/s); $\mathbf{u}$ is the Darcian flux ($m^3/m^2/s$); r_m is the total rate of kinetically controlled reactions that involve m [mol/(m^3 s)]; ss_m is the additional net sources/sinks [mol/(m^3 s)], which can include chemical species entering or leaving a finite volume through rainfall, dust deposition, and snowfall. Applying the semidiscrete approach by integrating over a three-dimensional control volume, the following ODE form of equation (6) is obtained for the prismatic element i:

$$V_i \frac{d(S_{w,i}\theta_i C_{m,i})}{dt} = \sum_{j=N_{i,1}}^{N_{i,x}} \left(A_{ij} D_{ij} \frac{C_{m,j} - C_{m,i}}{l_{ij}} - q_{ij} C_{m,j} \right) + R_{m,i} + SS_{m,i}, \quad (7)$$

where V_i is total volume of the element i; $N_{i,x}$ is the index of elements sharing surfaces with element i; the value of x is 2 for unsaturated zone (infiltration, recharge) and is 4 for saturated zone (recharge plus three lateral flow directions), respectively; A_{ij} is the grid interface area shared by element i and its neighbor element j; D_{ij} is the norm (m^2/s) of combined dispersion/diffusion tensor normal to the shared surface A_{ij}; l_{ij} is the distance between the center of the element i and its neighbor elements j; q_{ij} is the flow rate across shared surfaces A_{ij} (m^3/s), which includes the right hand side terms in equations (3–5): lateral flow rates, recharge rate and infiltration rate; $R_{m,i}$ is the total rate of kinetic-controlled reactions that involve m (mol/s); $SS_{m,i}$ is the additional total net sources (mol/s). The term $V_i\theta_i S_{w,i}$ represents the total water volume in each prismatic element i. Dividing the total water volume by base area A_i yields the total water storage of the element ($h_{u,i} + h_{g,i}$). We can further write equation (7) into two equations for concentrations of m in the unsaturated and saturated zones, the summation of which yields the mass conservation of the entire prismatic element in equation (7).

The surface water (overland flow) only exists during and immediately after rainfall and has very short interaction time with the land surface. Solute reactive transport in surface water is therefore not explicitly modeled in RT. Surface water is assumed to flow into the stream and infiltrate into the soil with chemical composition of the through fall. The stream water has both above and below ground components such that solutes go through reactive transport processes and are explicitly simulated with ADR equations in similar forms as equations (7).

Reaction rate laws. For kinetic-controlled mineral dissolution and precipitation, the rate is calculated based on the Transition State Theory (TST) [*Helgeson et al*., 1984b; *Lasaga*, 1984]:

$$R_k = A_{w,k} k_k \left(1 - \frac{IAP}{K_{eq}}\right). \quad (8)$$

Here R_k is the dissolution/precipitation rate of a mineral k [mol/(m^3 s)]; $A_{w,k}$ is the "wetted" dissolving surface area of mineral k per volume of porous media (m^2/m^3); k_k is the intrinsic rate constant [mol/(m^2 s)]; IAP is the ion activity product; and K_{eq} is the equilibrium constant of the reaction. The wetted mineral surface area strongly depends on soil moisture [*Clow and Mast*, 2010] and can be calculated as

$$A_{w,k} = A_k^0 S_w^n. \quad (9)$$

Here $A_k{}^0$ is the total mineral surface area per volume of porous media under fully saturated conditions. In this work, we use an n value of 2/3 to take into account the conversion between volume and area [*Mayer et al*., 2002]. Secondary minerals that have the potential to precipitate are assigned an initial value of 10^{-8} mol/m^3 porous media to allow for the occurrence of precipitation when conditions permit. Mineral dissolution stops when the mineral mass reaches this value. Activities of chemical species are calculated using the Debye-Hückel equation [*Debye and Hückel*, 1923]. Surface complexation and cation exchange reactions are modeled following the nonelectrostatic approach and Vanselow conventions, respectively [*Dzombak*, 1990; *Vanselow*, 1932].

2.5. Numerical Implementation

The Noah LSM simulates the internal soil moisture flux within the unsaturated zone using infiltration and recharge rates calculated from PIHM. PIHM solves lateral water flows and the exchange between unsaturated and saturated zones. The RT module follows a sequential noniterative approach (SNIA) that has been widely used [*Walsh et al*., 1984; *Yeh and Tripathi*, 1989] and is efficient in integrating subsurface flow simulation with reactive transport algorithms [*Jacques et al*., 2006]. The SNIA is derived from the operator-splitting method and decouples ADR equations and solves transport and reaction steps separately [*Xu et al*., 1999; *Zysset et al*., 1994]. The transport step is solved using the forward Euler method while the reaction step is solved iteratively using the Crank-Nicolson and Newton-Raphson method. In the reaction step, the local matrices accounting for the mass balance of all primary species in each finite volume are assembled and solved using a matrix solver in SUNDIALS [*Hindmarsh et al*., 2005]. Concentrations from previous time steps are used as the initial guess to iteratively solve for concentrations in the current time step.

The accuracy of the SNIA approach depends on multiple factors including spatial discretization, time stepping, and flow conditions. Performance index (PI) is used to optimize the time stepping and to minimize numerical errors and improve convergence. The PI is set to be less than 0.05 for every shared surface between elements to minimize the operator-splitting error associated with temporal discretization [*Jacques et al*., 2006; *Perrochet and Bérod*, 1993]:

$$\left(\frac{q_{ij}A_i}{A_{ij}}\right)^2 \frac{\Delta t}{D_{ij}} < 0.05. \tag{10}$$

Here Δt is the time duration in each step. The use of small PI and maximum time step requires a longer computational time however improves the SNIA accuracy.

The spatial heterogeneity in hydrological processes can cause significant nonconvergence problems. For example, flow rates between neighboring elements can vary from 0.01 to 4000 m^3/d. When flow rates are high, time steps are reduced to facilitate convergence. Reducing time steps based on the fastest flow, however, would essentially prevent the computation from marching forward. Therefore, sub time step interpolation is used in the fast-flow regime to obtain a closer initial guess when nonconvergence is encountered. During such interpolation, the time step in the kinetic reaction solver for a particular gird block is continuously decreased until a convergence is reached. The solver then proceeds using the reduced time step until it catches up the time step of the flow field. Numerical dispersion can be significant for large-scale transport simulations with large grid blocks and fast flow dominated by advection [*Li and Duffy*, 2012]. A total variation diminishing technique (TVD), which is third-order accurate in smooth regions, is used to reduce the extent of numerical dispersion [*Gupta et al*., 1991]. The RT module typically takes larger time steps than the default 1 min in the Flux-PIHM module. Flux values are stored and averaged before each RT time stepping.

The code generates unstructured grids based on Delaunay triangulation, considering constraints related to river network, watershed boundary, elevation contours, vegetation, and geology. Grids close to rivers and

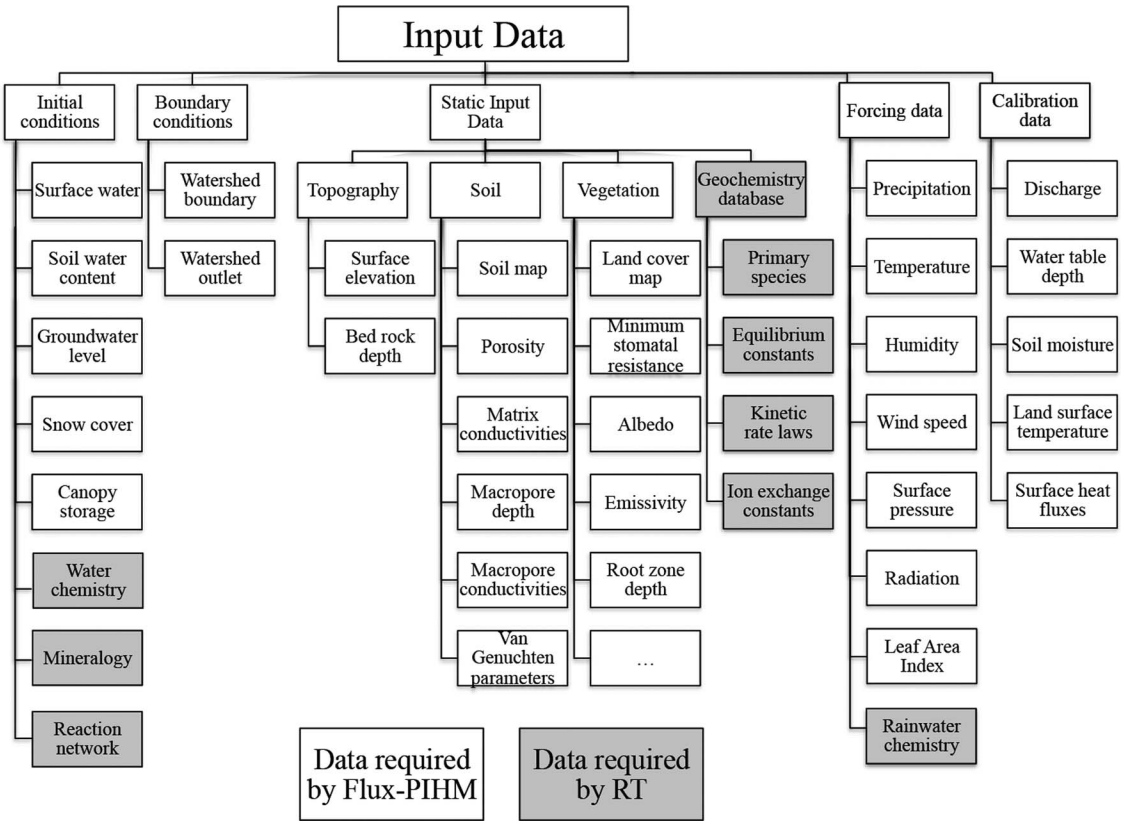

Figure 3. Five types of input files are required in RT-Flux-PIHM: initial conditions, boundary conditions, static inputs, forcing data, and calibration files. In addition to data required by Flux-PIHM, the RT module needs initial geochemical conditions, reaction networks, geochemical database, and forcing chemistry to simulate geochemical processes.

Table 1. Reactions and Thermodynamic and Kinetic Parameters [*Wolery*, 1992]

Aqueous Speciation	$\log_{10} K_{eq}$		
$CO_2(aq) + H_2O == H^+ + HCO_3^-$	−6.34		
$HCO_3^- == H^+ + CO_3^{2-}$	−10.33		
$H_2O == H^+ + OH^-$	−13.99		
Cation Ion Exchange	**$\log_{10} K_{eq}$**		**Site Density (mol/m^2)**
$>XNa + H^+ \leftrightarrow >HX + Na^+$	2.40		1×10^{-4}
$>X_2Ca + 2Na^+ \leftrightarrow >2NaX + Ca^{2+}$	0.50		
$>X_2Mg + 2Na^+ \leftrightarrow >2NaX + Mg^{2+}$	0.50		
Kinetic Reaction	**$\log_{10} K_{eq}$**	**$\log_{10} k$ (mol/m^2/s)**	**Specific Surface Area (SSA, m^2/g)**
$Calcite + H^+ == Ca^{2+} + HCO_3^-$	1.85	−9.19	0.01

steep areas are typically small and those in flat, less dynamic areas are large. For the small Shale Hills Critical Zone Observatory (SSHCZO) of 0.08 km^2, a total of 535 prismatic elements in the land and 20 stream segments is used with typical mesh sizes between 10 and 100 m. The standalone Flux-PIHM component solves for the land-surface hydrological processes for 1 year within 3 h with 1 min time steps on an Intel® Xeon® CPU E5-2670 @ 2.60GHz. Depending on the complexity of reaction networks and external forcing, the simulation time for RT-Flux-PIHM for 1 year of watershed processes varies between hours to days. The computational expense is expected to increase if the code is applied to large watersheds maintaining similar resolution, particularly because of the nonlinear nature of geochemical reactions. The code, however, has

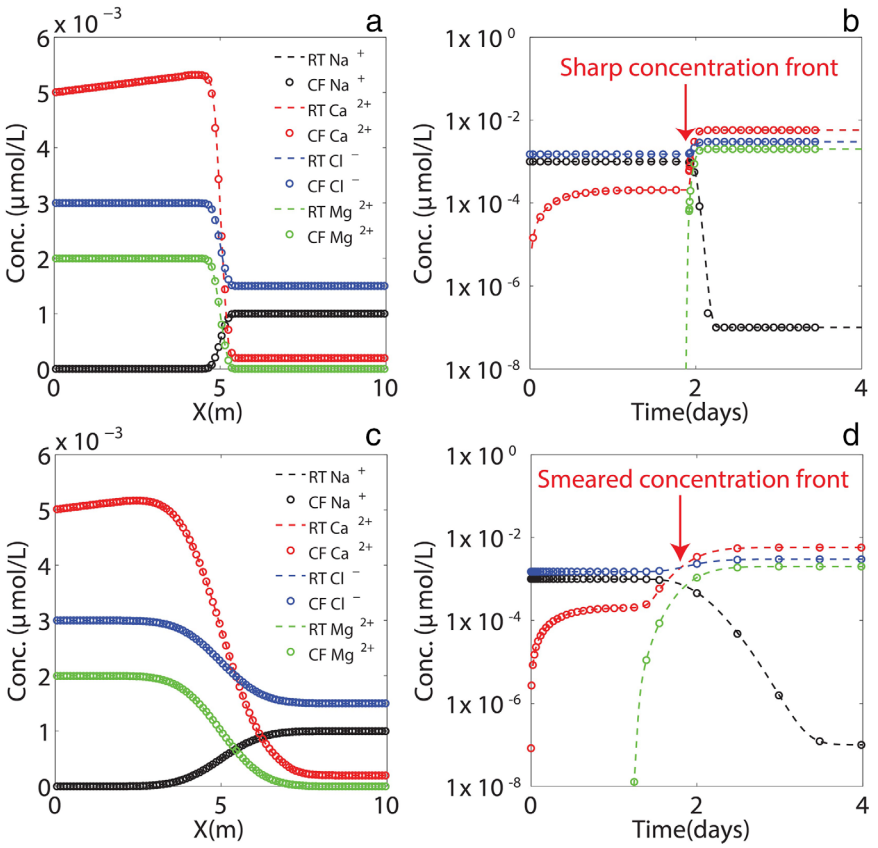

Figure 4. Comparison of model outputs from RT and CrunchFlow for the advection-only case (top row) and the case with advection, diffusion, and dispersion (bottom row). (a, c) Spatial distribution of solutes on day 1 (half residence time); (b, d) breakthrough curves (BTC). RT and CF generate almost identical results except some slight differences at the sharp concentration front. Initially, magnesium is all on the exchange sites so no magnesium broke through before 1.9 days. The sharp front suggests good remediation of numerical dispersion in both codes.

been applied to much larger watersheds, including the Mahantango Creek watershed in the Susquehanna River Basin with a drainage area of approximately 430 km^2 with thousands of grid blocks [*Bhatt et al*., 2014].

2.6. Data Requirements, Model Input, and Output

To physically simulate these dynamic processes, multiple types of input data are required (Figure 3). PIHM-gis, a tightly coupled GIS interface to PIHM, is used to set up model domains. The data infrastructure Hydro-Terre Data System (http://www.hydroterre.psu.edu) harvests, aggregates, and preprocesses essential terrestrial data from federal agencies (e.g., NED and NLCD) [*Bhatt et al*., 2014]. Flux-PIHM takes in watershed characteristics, initial conditions and boundary conditions, and time series forcing data. Watershed characteristics include topography (e.g., soil depth, surface elevation), soil properties (e.g., soil type, soil hydraulic conductivity, porosity, macropore conductivity, van Genuchten parameters), and vegetation properties (e.g., land cover type, rooting depth, maximum stomatal resistance). Watershed initial and boundary conditions include initial water distribution, soil temperature, land-surface temperature, water table depth, snow cover, canopy storage and watershed boundary fluxes. Time series forcing data include precipitation, air temperature, relative humidity, wind speed, downward solar radiation, downward longwave radiation, surface air pressure, and leaf area index (LAI). RT takes in the geochemistry of rainwater, soil water, soils, as well as thermodynamics and kinetics of geochemical reactions. A set of control and calibration files is required to facilitate the history matching using the global calibration coefficient approach [*Pokhrel and Gupta*, 2010]. Calibration is not built in the model. The history matching typically requires calibration for physical parameters such as soil hydraulic properties, and geochemical parameters including reactive surface area.

3. Model Verification for RT Module

To verify the implementation of RT, we compare its solutions to the extensively used reactive transport code CrunchFlow under a variety of flow and reaction conditions [*Steefel and Lasaga*, 1994]. Here we show one example of model verification. The OS3D mode is used in CrunchFlow with the total variation diminishing (TVD) option. A column of 10 cm is set up with calcite (10 vol %) and nonreactive minerals (90 vol %) and is injected with acidic solution at a pH of 4.0. In total, the system has six primary species (H^+, HCO_3^-, Ca^{2+}, Mg^{2+}, Na^+, Cl^-), three secondary species (OH^-, CO_3^{2-}, CO_2(aq)), one kinetic reaction (calcite dissolution), and one ion exchange reaction at equilibrium (Table 1).

In the advection-only case where diffusion coefficient (1.0×10^{-20} cm^2/s) and dispersivity (1.0×10^{-20} m) are set to be negligible, we test the code capability to capture the sharp concentration front. In another case, we include diffusion and dispersion processes with a diffusion coefficient of 1.0×10^{-5} cm^2/s and a dispersivity of 0.1 m while maintaining all other conditions the same as the advection-only case [*Gelhar et al*., 1992]. In both cases, the flow velocity is 2.0 m/d (with porosity = 0.4, the seepage velocity is 5.0 m/d). The number of grid blocks is 100 with a grid resolution of 0.1 cm. In the advection-only case, both codes successfully capture the sharp concentration fronts. Solutions from RT and CrunchFlow have relative differences of less than 10^{-8} in the smooth regions and relative differences in the order of $<10^{-4}$ at the sharp front. For the case with diffusion and dispersion, solutions from the two codes are identical with relative error less than 10^{-8} everywhere (Figure 4).

4. Model Demonstration

In this section, we demonstrate the application of RT-Flux-PIHM in understanding the hydrogeochemical processes in SSHCZO, a V-shaped, first-order watershed in central Pennsylvania [*Duffy et al*., 2009; *Jin et al*., 2011; *Qu and Duffy*, 2007]. We focus on water dynamics and export of the nonreactive tracer Cl (mostly originated from rainfall) and reactive Mg (derived from clay dissolution) during a large rainfall event. Large rainfall events are defined as those with intense precipitation within a relatively short period of time. These events are expected to significantly influence reactions and transport at the watershed scale [*McGuire and McDonnell*, 2010; *Torres et al*., 2015]. The concentration (C) and discharge (Q) hysteresis, i.e., differing solute concentrations at the same stream discharge rates during the rising and recession limbs of single rainfall events, has often been observed and has been frequently used as signatures of water dynamics and geochemical processes in catchments [*Abell et al*., 2013; *Evans and Davies*, 1998; *Evans et al*., 1999; *Hendrickson and Krieger*, 1964; *House and Warwick*, 1998; *Toler*, 1965]. The orientation and looping direction of CQ

Table 2. Reactions and Thermodynamics and Kinetics

Chlorite Dissolution	$\log_{10} K_{eq}$	$\log_{10} k$ (mol/m^2/s)	Specific Surface Area (SSA, m^2/g)
$(Fe_{0.24}Mg_{0.38}Al_{0.38})_6(Si_{0.07}Al_{0.93})_4O_{10}(OH)_{8(s)}$ (chlorite) + $5.72H_4SiO_{4(aq)}$ + $4.56H^+ \rightarrow 1.44FeOOH_{(s)} + 2.28Mg^{2+} + 3Al_2Si_2O_5(OH)_{4(s)} + 11H_2O$	38.8	−12.5[a]	0.01 (1.1–7.7)[a]
Cation Exchange Reaction	$\log_{10} K_{eq}$		Site Density[b] (meq/g)
$>XNa + H^+ \leftrightarrow >HX + Na^+$	2.40		
$>X_2Ca + 2Na^+ \leftrightarrow >2NaX + Ca^{2+}$	0.50		30.0–0.70
$>X_2Mg + 2Na^+ \leftrightarrow >2NaX + Mg^{2+}$	0.50		

[a]Values in parentheses for comparison from *Aylmore et al*. [1970] and *Köhler et al*. [2003, 2005].
[b]Derived from *Jin et al*. [2010] using Vanselow convention [*Vanselow*, 1932].

hysteresis have been interpreted as controlled by the timing and contribution from source waters of varying chemical composition including surface runoff, soil water flow, and groundwater flow [*Chanat et al*., 2002; *Christophersen et al*., 1990; *Duffy and Cusumano*, 1998; *Hooper et al*., 1990; *McGlynn and McDonnell*, 2003]. Clockwise loops typically indicate quick mobilization from surface runoff [*Abell et al*., 2013; *Bowes et al*., 2005], while anticlock loops imply a delay in solute arrival time due to slow diffusion or long travel time through subsurface [*Abell et al*., 2013; *Bowes et al*., 2005; *Cerro et al*., 2014]. In general, the role of ion exchange (and geochemical processes in general) in determining the characteristics of hysteresis loop has rarely been explored and is not well understood [*Clow and Mast*, 2010].

Here we aim to understand the role of ion exchange in determining solute CQ hysteresis by comparing two simulation cases. In one case, Mg dissolves from chlorite but does not participate in ion exchange (w/o CEC). In another case, dissolved Mg also participates in ion exchange reactions (w/CEC). The discussion is kept relatively brief to illustrate the salient capabilities of RT-Flux-PIHM in understanding hydrogeochemical coupling. More detailed applications and in-depth discussion are in the companion paper [*Li et al*., 2017b].

4.1. Model Setup

RT-Flux-PIHM allows watershed initialization with spatial heterogeneity in both physical and chemical properties. Extensive field surveys have provided spatial distribution of the topographic and hydrological properties. Here we use the spatial distribution of measured soil thickness, soil elevation, soil series, and mineralogy [*Jin and Brantley*, 2011; *Jin et al*., 2010; *Lin*, 2006]. Prior to this work, parameters for hydrological land-surface processes have been carefully calibrated using multiple field measurements (discharge, soil moisture, water table depth, and surface heat fluxes) in 2009 [*Shi et al*., 2013].

Note that RT is coded as a general purpose RTM code where reaction networks, thermodynamics, and kinetics can be defined in input and database files. In SSHCZO, chloride originates from atmospheric deposition. Chlorite dissolution in the shallow regolith releases magnesium [*Jin et al*., 2014]. Magnesium also participates in cation exchange reaction [*Jin et al*., 2010] (Table 2). Note that the specific surface area of chlorite dissolution is more than 3 orders of magnitude lower than rate constants measured in well-mixed reactors. This is to take into account the fact that at the grid block scale of 10–100 m, the effectively reacting surface areas are often orders of magnitude lower than those measured for grounded mineral grains [*Moore et al*., 2012; *Salehikhoo and Li*, 2015; *White and Brantley*, 2003]. The primary species here are H^+, HCO_3^-, and cations from chlorite dissolution. Aqueous complexation reactions are considered with secondary species OH^-, CO_2(aq), CO_3^{2-}, $MgCO_3$(aq), $MgCl^+$, and $MgHCO_3^+$.

4.2. Water and Solute Dynamics

Here we simulate water and geochemical dynamics in SSHCZO during a large rainfall event on 24 October 2009. As shown in Figures 5a and 5b, during the rainfall event, water storage increases due to infiltration and recharge. The stream is therefore connected to a larger portion of the watershed than under the dry conditions before the rainfall. Water storage in the unsaturated zone quickly restores to its prerainfall level; water storage in the saturated zone however sees elevated values after 4 days following the rainfall event, reflecting much slower fluxes out of the saturated zone. The Cl concentration ([Cl]) in soil water is relatively high before the event and is flushed out quickly during the event and becomes much more homogeneously distributed afterward (Figure 5c). For magnesium, the spatial distribution of the water content (dictated

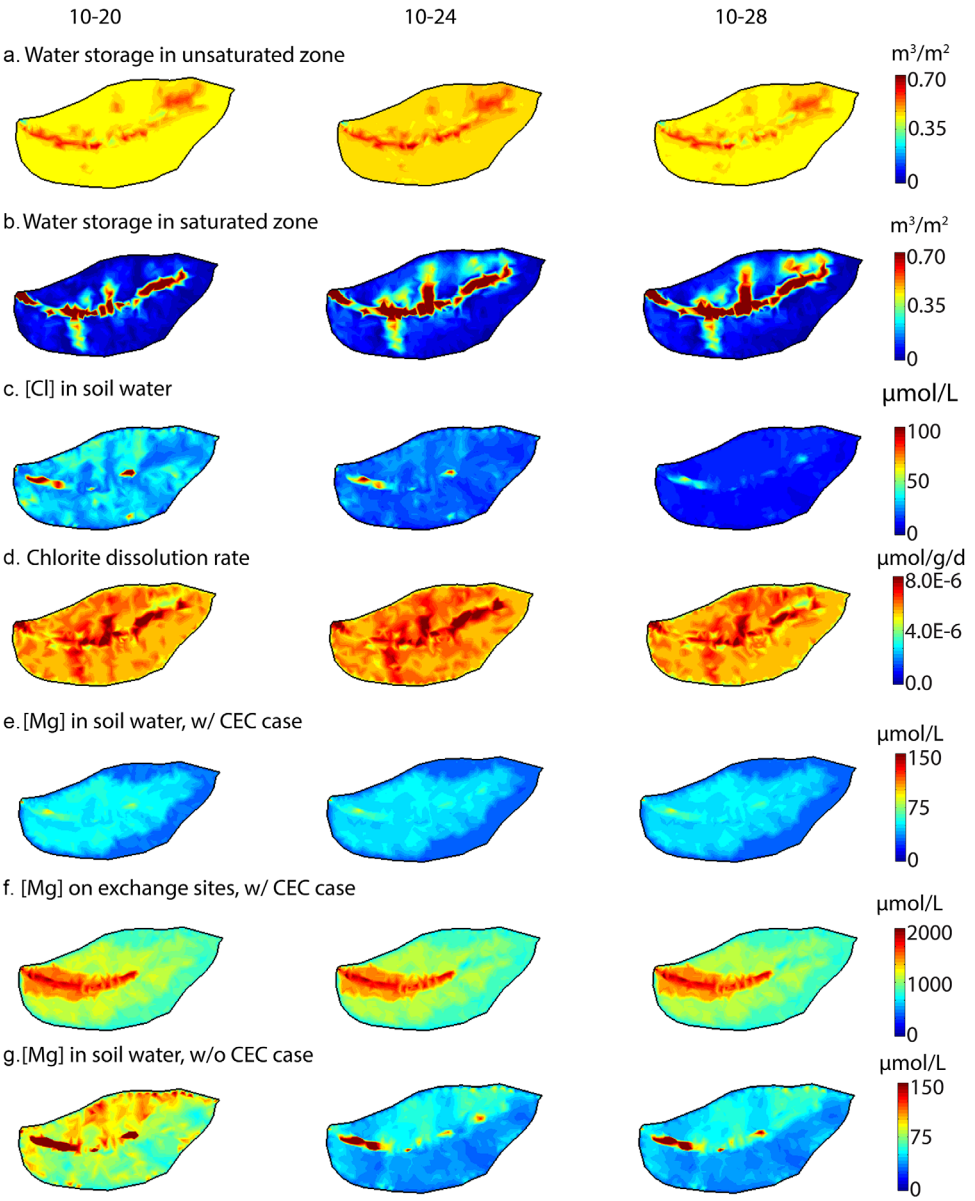

Figure 5. Spatial profiles of water and solutes before, during, and after the rainfall event on 24 October 2009. (a) Water storage h_u in the unsaturated zone (m^3/m^2); (b) water storage h_g in the saturated zone (m^3/m^2); (c) [Cl] (μmol/L-soil water); (d) chlorite dissolution rates (μmol/g-soil/d); (e) [Mg] in soil water for w/CEC case (μmol/L-soil water); (f) Mg on exchange sites, w/CEC case (μmol/L-soil water); (g) [Mg] in soil water for w/o CEC case (μmol/L-soil water).

by topography) determines the highs and lows of local chlorite dissolution rates: higher dissolution rates and Mg concentrations occur in swales and valley floor where water flow converges. Chlorite dissolution rates during the rainfall are in general higher with high water content (Figure 5d). Comparing the cases with and without ion exchange, the spatiotemporal variation of local Mg concentrations ([Mg]) in soil water is relatively small with the presence of ion exchange (Figures 5e and 5f). The soil surface in the w/CEC case stores much more Mg than soil water and serves as a large buffering reservoir. Without cation exchange (Figure 5g), [Mg] in soil water drops quickly and is more responsive to the rainfall event due to the lack of ion exchange buffering capacity. In this case, Mg behaves similarly to Cl, although it is derived from chlorite dissolution while Cl comes from the rainfall.

Figure 6 shows the model output of solute concentrations and fluxes from the stream mouth in days before, during, and after the large rainfall event. Before the large rainfall event, the relatively dry watershed has

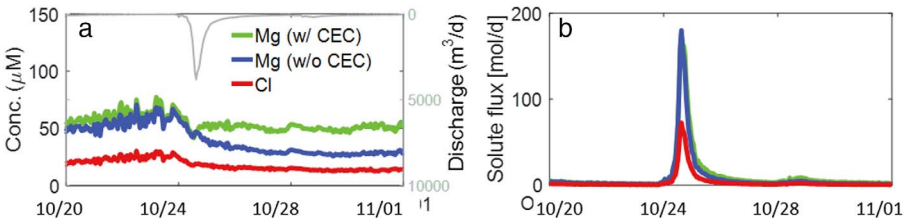

Figure 6. Predicted hourly discharge, concentrations in stream water, and fluxes as a function of time before and after a large rainfall event on 24 October 2009. (a) Discharge, [Cl], [Mg] (w/CEC and w/o CEC) in stream water. (b) Solute efflux in discharge.

high solute concentrations with large spatial variation (e.g., 20 October, Figure 5). A few small rainfall events (not shown) before the large rainfall event lead to the "zigzags" of the discharge concentrations, as shown in Figure 6a. The solute concentrations however quickly drop and become more stable as the rainfall intensifies to its peak. After that, although discharge decreases by more than 2 orders of magnitude from ~50 to 4000 m^3/d, solute concentrations at the stream outlet are relatively stable. In the case without ion exchange, stream Mg drops to approximately half of its preevent concentration, behaving similarly to Cl. In contrast, ion exchange keeps [Mg] relatively constant without as much drop because Mg releases from exchange sites, compensating for the dilution of Mg by higher water content. As shown in Figure 6b, solute export rates are orders of magnitude higher during the large rainfall event, highlighting the significance of large rainfall in exporting solutes from the land to the stream.

4.3. The Role of Ion Exchange on CQ Hysteresis

Figure 7 shows hourly model output of stream concentration and discharge (CQ relationship) between 22 October and 26 October 2009. Simulation results show that Cl is flushed out in early stage of the event (Figures 6a and 7). The rainfall quickly dilutes and reduces [Cl]. The Cl concentrations are different at low discharges of rising and recession limbs. Magnesium behaves very similarly to Cl without cation exchange (w/o CEC), except that its concentrations are generally higher and the hysteresis exists for a larger discharge range. Concentrations of Cl and Mg do not return to their preevent level so no hysteresis loop is formed. Postevent concentrations after the large rainfall are lower because water flushes out solutes.

With cation exchange, Mg exhibits hysteresis loop. The [Mg] in the rising limb is lower than that in the recession limb (Figure 7, green line) and is similar to [Mg] in the rising limb without cation exchange case. This indicates that surface runoff with low [Mg] reaches the stream quickly and dominates the stream discharge during the rising limb such that ion exchange does not make a difference. During the recession limb, however, the discharge primarily comes from subsurface lateral flow carrying higher [Mg] released from ion exchange, therefore leading to higher concentrations in the stream. The [Mg] difference in the rising and recession limbs is about 10 μM and is small compared to the more than 2 orders of magnitude variation in discharge. Cation exchange acts as a buffer and restores [Mg] to the prerainfall level, forming a closed CQ hysteresis loop.

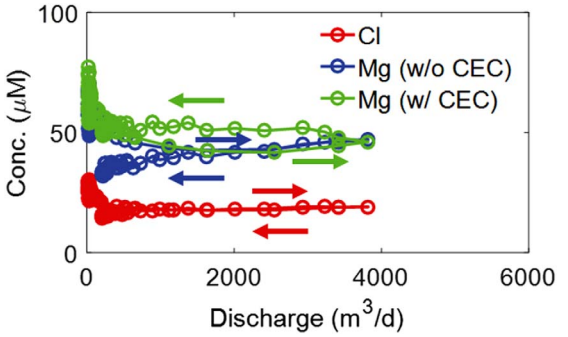

Figure 7. Concentration-discharge plots for Cl and Mg from hourly output of RT-Flux-PIHM simulation from 22 to 26 October 2009. Colored arrows indicate the rising limb (arrow pointing to the right) and recession limb (arrow pointing to the left). For Mg, the CQ curve without CEC (w/o CEC) is very similar to that of Cl. Mg CQ curve with CEC shows higher concentration in the recession limb and closed hysteresis loop, indicating delayed arrival of Mg from soil exchange sites.

The counter-clock hysteresis loop of Mg here corresponds to the A3 type defined by *Evans and Davies* [1998], where solute concentrations in soil water or ground water are higher than those in surface runoff. Note that in the model there is no deeper groundwater so there are two end-members: surface runoff and soil water from subsurface lateral water. This indicates that although a groundwater component is not present, A3 type hysteresis can still occur with cation exchange reaction.

Ion exchange mobilizes cations from soil surfaces and elevates stream concentrations in the later stage of the rainfall event, which has not been shown previously.

5. Conclusion

In this work, we developed RT-Flux-PIHM, a new physics-based code that integrates land-surface, hydrological and multicomponent reactive transport processes at the watershed scale. The model capability is illustrated through an example examining the role of ion exchange in determining the concentration-discharge relationship of the nonreactive Cl and the reactive solute Mg during a large rainfall event. The model shows that watershed topography dictates where, when, and how much water flows and soil dissolves. The large rainfall wets and connects the watershed, leading to relatively homogeneous distribution of solutes after the event. The ion exchange process of Mg buffers and maintains almost constant Mg concentration in stream water, leading to a counter-clockwise concentration-discharge hysteresis loop during a large rainfall event. Without ion exchange, Mg behaves similarly to the nonreactive Cl, although Mg comes from chlorite dissolution while Cl is from wet deposition.

Watershed is the fundamental hydrological unit that connects the terrestrial to aquatic systems [*Grimm et al*., 2003]. Understanding how solutes react and move between the land and streams is important for estimating chemical loads into river networks and eventually into the ocean, for quantifying biogeochemical rates, of and for predicting responses and feedbacks of earth surface systems to the changing climate. RT-Flux-PIHM can be used to carry out virtual experiments to understand, quantify, and predict hydrogeochemical processes under a variety of climate, topography, and geochemical conditions. With the complexity of processes and watershed characteristics, it inevitably suffers from similar limitation as distributed hydrology models including nonuniqueness and equifinality [*Beven and Freer*, 2001; *Beven*, 2000]. In addition, parameter uncertainty and sensitivity remain a significant challenge [*Neuman et al*., 2012; *Song et al*., 2015; *Ye et al*., 2008]. It however provides capabilities for teasing apart the importance of individual processes, for mechanistically understanding emergent behavior, and for predicting process coupling and feedbacks in complex systems. In addition, vast surface and subsurface water and biogeochemistry data have become available through efforts coordinated through large research community networks including the Critical Zone Observatories (CZOs), Long Term Ecological Research (LTER) network, and United Stated Geological Survey (USGS). These complex data sets can be integrated into complex modeling tools such as RT-Flux-PIHM to answer fundamental questions across hydrology and geochemistry, as illustrated in the companion paper [*Li et al*., 2017a].

Acknowledgments

This work is supported by NSF Critical Zone Observatory program grants to C.J.D. (EAR 07-25019) and S.L.B. (EAR 12-39285, EAR 13-31726). Data used in this research were collected in Penn State's Stone Valley Forest, which is supported and managed by the Penn State's Forestland Management Office in the College of Agricultural Sciences. These data have been digitized and are accessible through national CZO data portal (http://criticalzone.org/shale-hills/data/datasets/). All data are available at the Interdisciplinary Earth Data Alliance (IEDA) website [*Brantley and Sullivan*, 2014; *Brantley et al*., 2013]. The source code of RT-Flux-PIHM and the input files necessary to reproduce the results are available from the authors upon request (lili@engr.psu.edu). We appreciate the Associate Editor Ming Ye and the Editor Jean Bahr for handling the manuscript and for providing insightful feedbacks on how to improve the manuscript. We acknowledge Jon Chorover, Gene-Hua Crystal Ng, and three anonymous reviewers for their constructive and meticulous reviews that have improved the paper.

References

Abell, J. M., D. P. Hamilton, and J. C. Rutherford (2013), Quantifying temporal and spatial variations in sediment, nitrogen and phosphorus transport in stream inflows to a large eutrophic lake, *Environ. Sci. Processes Impacts*, *15*(6), 1137–1152.

Arnold, J. G., R. Srinivasan, R. S. Muttiah, and J. R. Williams (1998), Large area hydrologic modeling and assessment: Part i: Model development 1, *J. Am. Water Resour. Assoc.*, *34*(1), 73–89.

Audigane, P., I. Gaus, I. Czernichowski-Lauriol, K. Pruess, and T. Xu (2007), Two-dimensional reactive transport modeling of CO_2 injection in a saline aquifer at the Sleipner site, North Sea, *Am. J. Sci.*, *307*(7), 974–1008.

Aylmore, L., I. Sills, and J. Quirk (1970), Surface area of homoionic illite and montmorillonite clay minerals as measured by the sorption of nitrogen and carbon dioxide, *Clays Clay Miner.*, *18*(2), 91–96.

Bao, C., H. Wu, L. Li, D. Newcomer, P. E. Long, and K. H. Williams (2014), Uranium bioreduction rates across scales: Biogeochemical hot moments and hot spots during a biostimulation experiment at rifle, Colorado, *Environ. Sci. Technol.*, *48*(17), 10,116–10,127.

Beaulieu, E., Y. Goddéris, D. Labat, C. Roelandt, D. Calmels, and J. Gaillardet (2011), Modeling of water-rock interaction in the Mackenzie basin: Competition between sulfuric and carbonic acids, *Chem. Geol.*, *289*(1–2), 114–123.

Beisman, J., R. Maxwell, A. Navarre-Sitchler, C. Steefel, and S. Molins (2015), ParCrunchFlow: An efficient, parallel reactive transport simulation tool for physically and chemically heterogeneous saturated subsurface environments, *Comput. Geosci.*, *19*, 403–422.

Bethke, C. (1996), *Geochemical Reaction Modeling: Concepts and Applications*, 397 pp., Oxford Univ. Press, New York.

Beven, K. (1989), Changing ideas in hydrology—The case of physically-based models, *J. Hydrol.*, *105*(1), 157–172.

Beven, K., and J. Freer (2001), Equifinality, data assimilation, and uncertainty estimation in mechanistic modelling of complex environmental systems using the GLUE methodology, *J. Hydrol.*, *249*(1–4), 11–29.

Beven, K., and P. Germann (1982), Macropores and water flow in soils, *Water Resour. Res.*, *18*(5), 1311–1325.

Beven, K. J. (2000), Uniqueness of place and process representations in hydrological modelling, *Hydrol. Earth Syst. Sci.*, *4*(2), 203–213.

Bhatt, G., M. Kumar, and C. J. Duffy (2014), A tightly coupled GIS and distributed hydrologic modeling framework, *Environ. Modell. Software*, *62*, 70–84.

Bishop, K., J. Seibert, S. Köhler, and H. Laudon (2004), Resolving the Double Paradox of rapidly mobilized old water with highly variable responses in runoff chemistry, *Hydrol. Processes*, *18*(1), 185–189.

Bolton, E. W., A. C. Lasaga, and D. M. Rye (1996), A model for the kinetic control of quartz dissolution and precipitation in porous media flow with spatially variable permeability: Formulation and examples of thermal convection, *J. Geophys. Res.*, *101*(B10), 22,157–22,187.
Boone, A. A., F. Habets, J. Noilhan, D. Clark, P. Dirmeyer, S. Fox, Y. Gusev, I. Haddeland, R. Koster, and D. Lohmann (2004), The Rhone-aggregation land surface scheme intercomparison project: An overview, *J. Clim.*, *17*(1), 187–208.
Bowes, M. J., W. A. House, R. A. Hodgkinson, and D. V. Leach (2005), Phosphorus-discharge hysteresis during storm events along a river catchment: The River Swale, UK, *Water Res.*, *39*(5), 751–762.
Boyer, E. W., G. M. Hornberger, K. E. Bencala, and D. M. McKnight (1997), Response characteristics of DOC flushing in an alpine catchment, *Hydrol. Processes*, *11*(12), 1635–1647.
Brantley, S. L., and M. Lebedeva (2011), Learning to read the chemistry of regolith to understand the critical zone, in *Annual Review of Earth and Planetary Sciences*, vol. 39, edited by R. Jeanloz and K. H. Freeman, pp. 387–416.
Brantley, S. L., and P. L. Sullivan (2014), *Susquehanna Shale Hills Critical Zone Observatory Porewater Chemistry (2011)*, Integrated Earth Data Appl. [Available at http://www.iedadata.org/.]
Brantley, S. L., L. Jin, D. Andrews, G. Holmes, M. Holleran, J. Z. Williams, E. Herndon, and P. L. Sullivan (2013), *Susquehanna Shale Hills Critical Zone Observatory Porewater Chemistry (2008)*, Integrated Earth Data Appl.
Brooks, P. D., J. Chorover, Y. Fan, S. E. Godsey, R. M. Maxwell, J. P. McNamara, and C. Tague (2015), Hydrological partitioning in the critical zone: Recent advances and opportunities for developing transferrable understanding of water cycle dynamics, *Water Resour. Res.*, *51*, 6973–6987, doi:10.1002/2015WR017039.
Brunet, J.-P.L., L. Li, Z. T. Karpyn, and N. J. Huerta (2016), Fracture opening or self-sealing: Critical residence time as a unifying parameter for cement-CO_2-brine interactions, *Int. J. Greenhouse Gas Control*, *47*, 25–37.
Cerro, I., J. M. Sanchez-Perez, E. Ruiz-Romera, and I. Antigueedad (2014), Variability of particulate (SS, POC) and dissolved (DOC, NO_3) matter during storm events in the Alegria agricultural watershed, *Hydrol. Processes*, *28*(5), 2855–2867.
Chanat, J. G., K. C. Rice, and G. M. Hornberger (2002), Consistency of patterns in concentration-discharge plots, *Water Resour. Res.*, *38*(8), doi:10.1029/2001WR000971.
Chapman, B. M. (1982), Numerical simulation of the transport and speciation of nonconservative chemical reactants in rivers, *Water Resour. Res.*, *18*(1), 155–167.
Chapman, B. M., R. O. James, R. F. Jung, and H. G. Washington (1982), Modelling the transport of reacting chemical contaminants in natural streams, *Mar. Freshwater Res.*, *33*(4), 617–628.
Chen, F., and J. Dudhia (2001), Coupling an advanced land surface-hydrology model with the Penn State-NCAR MM5 modeling system. Part I: Model implementation and sensitivity, *Mon. Weather Rev.*, *129*(4), 569–585.
Christophersen, N., C. Neal, R. P. Hooper, R. D. Vogt, and S. Andersen (1990), Modelling streamwater chemistry as a mixture of soilwater end-members—A step towards second-generation acidification models, *J. Hydrol.*, *116*(1–4), 307–320.
Clow, D. W., and M. A. Mast (2010), Mechanisms for chemostatic behavior in catchments: Implications for CO_2 consumption by mineral weathering, *Chem. Geol.*, *269*(1–2), 40–51.
Craig, L., J. M. Bahr, and E. E. Roden (2010), Localized zones of denitrification in a floodplain aquifer in southern Wisconsin, USA, *Hydrogeol. J.*, *18*(8), 1867–1879.
Dale, A. W., P. Regnier, N. J. Knab, B. B. Jorgensen, and P. Van Cappellen (2008), Anaerobic oxidation of methane (AOM) in marine sediments from the Skagerrak (Denmark): II. Reaction-transport modeling, *Geochim. Cosmochim. Acta*, *72*(12), 2880–2894.
Davison, J., H. Hwang, E. Sudicky, and J. Lin (2014), Development of a fully integrated water cycle model: HydroGeoSphere-Weather Research and Forecasting (HGS-WRF), Abstract xxxxx-xxxx presented at 2014 Fall Meeting, AGU.
Debye, P., and E. Hückel (1923), De la théorie des électrolytes. i. abaissement du point de congélation et phénomènes associés, *Phys. Z.*, *24*(9), 185–206.
Donigian, A., Jr., B. Bicknell, J. Imhoff, and V. Singh (1995), Hydrological Simulation Program-Fortran (HSPF), in *Computer Models of Watershed Hydrology*, pp. 395–442.
Druhan, J. L., C. I. Steefel, S. Molins, K. H. Williams, M. E. Conrad, and D. J. DePaolo (2012), Timing the onset of sulfate reduction over multiple subsurface acetate amendments by measurement and modeling of sulfur isotope fractionation, *Environ. Sci. Technol.*, *46*(16), 8895–8902.
Duffy, C., Y. Shi, K. Davis, R. Slingerland, L. Li, P. Sullivan, Y. Goddéris, and S. L. Brantley (2014), Designing a suite of models to explore critical zone function, *Procedia Earth Planet. Sci.*, *10*, 7–15.
Duffy, C. J. (2004), Semi-discrete dynamical model for mountain-front recharge and water balance estimation, Rio Grande of Southern Colorado and New Mexico, in *Groundwater Recharge in a Desert Environment: The Southwestern United States*, pp. 255–271.
Duffy, C. J., and J. Cusumano (1998), A low-dimensional model for concentration-discharge dynamics in groundwater stream systems, *Water Resour. Res.*, *34*(9), 2235–2247.
Dzombak, D. A. (1990), *Surface Complexation Modeling: Hydrous Ferric Oxide*, 393 pp., John Wiley, New York.
Ek, M. B., K. E. Mitchell, Y. Lin, E. Rogers, P. Grunmann, V. Koren, G. Gayno, and J. D. Tarpley (2003), Implementation of Noah Land Surface Model advances in the National Centers for Environmental Prediction operational mesoscale Eta model, *J. Geophys. Res.*, *108*(D22), 8851, doi:10.1029/2002JD003296.
Evans, C., and T. D. Davies (1998), Causes of concentration/discharge hysteresis and its potential as a tool for analysis of episode hydrochemistry, *Water Resour. Res.*, *34*(1), 129–137.
Evans, C., T. D. Davies, and P. S. Murdoch (1999), Component flow processes at four streams in the Catskill Mountains, New York, analysed using episodic concentration/discharge relationships, *Hydrol. Processes*, *13*(4), 563–575.
Fang, Y., T. D. Scheibe, R. Mahadevan, S. Garg, P. E. Long, and D. R. Lovley (2011), Direct coupling of a genome-scale microbial in silico model and a groundwater reactive transport model, *J. Contam. Hydrol.*, *122*(1–4), 96–103.
Freeze, R. A., and R. Harlan (1969), Blueprint for a physically-based, digitally-simulated hydrologic response model, *J. Hydrol.*, *9*(3), 237–258.
Gaillardet, J., B. Dupré, P. Louvat, and C. J. Allègre (1999), Global silicate weathering and CO_2 consumption rates deduced from the chemistry of large rivers, *Chem. Geol.*, *159*(1–4), 3–30.
Gan, T. Y., Y. Gusev, S. J. Burges, O. Nasonova, V. Andréassian, A. Hall, N. Chahinian, and J. Schaake (2006), Performance comparison of a complex physics-based land surface model and a conceptual, lumped-parameter hydrological model at the basin-scale, in *Large Sample Basin Experiments for Hydrological Model Parameterization: Results of the Model Parameter Experiment (MOPEX)*, pp. 196–208.
Gelhar, L. W., C. Welty, and K. R. Rehfeldt (1992), A critical review of data on field-scale dispersion in aquifers, *Water Resour. Res.*, *28*(7), 1955–1974.
Godderis, Y., L. M. Francois, A. Probst, J. Schott, D. Moncoulon, D. Labat, and D. Viville (2006), Modelling weathering processes at the catchment scale: The WITCH numerical model, *Geochim. Cosmochim. Acta*, *70*, 1128–1147.

Goddéris, Y., S. L. Brantley, L. M. Francois, J. Schott, D. Pollard, M. Deque, and M. Dury (2013), Rates of consumption of atmospheric CO_2 through the weathering of loess during the next 100 yr of climate change, *Biogeosciences*, *10*(1), 135–148.
Godsey, S. E., J. W. Kirchner, and D. W. Clow (2009), Concentration–discharge relationships reflect chemostatic characteristics of US catchments, *Hydrol. Processes*, *23*(13), 1844–1864.
Gottardi, G., and M. Venutelli (1993), A control-volume finite-element model for two-dimensional overland flow, *Adv. Water Resour.*, *16*(5), 277–284.
Grimm, N. B., et al. (2003), Merging aquatic and terrestrial perspectives of nutrient biogeochemistry, *Oecologia*, *137*(4), 485–501.
Gupta, A. D., L. Lake, G. Pope, K. Sepehrnoori, and M. King (1991), High-resolution monotonic schemes for reservoir fluid flow simulation, *In Situ*, *15*(3). *In Situ; (United States)*, Medium: X; Size, pp. 289–317.
Hammond, G., P. Lichtner, and R. Mills (2014), Evaluating the performance of parallel subsurface simulators: An illustrative example with PFLOTRAN, *Water Resour. Res.*, *50*, 208–228, doi:10.1002/2012WR013483.
Helgeson, H. C., W. M. Murphy, and P. Aagaard (1984a), Thermodynamic and kinetic constraints on reaction-rates among minerals and aqueous-solutions. 2. Rate constants, effective surface-area, and the hydrolysis of feldspar, *Geochim. Cosmochim. Acta*, *48*(12), 2405–2432.
Helgeson, H. C., W. M. Murphy, and P. Aagaard (1984b), Thermodynamic and kinetic constraints on reaction rates among minerals and aqueous solutions. II. Rate constants, effective surface area, and the hydrolysis of feldspar, *Geochim. Cosmochim. Acta*, *48*(12), 2405–2432.
Hendrickson, G. E., and R. A. Krieger (1964), *Geochemistry of Natural Waters of the Blue Grass Region, Kentucky*, U.S. Gov. Print. Off.
Hindmarsh, A. C., P. N. Brown, K. E. Grant, S. L. Lee, R. Serban, D. E. Shumaker, and C. S. Woodward (2005), SUNDIALS: Suite of nonlinear and differential/algebraic equation solvers, *ACM Trans. Math. Software*, *31*(3), 363–396.
Hooper, R. P., N. Christophersen, and N. E. Peters (1990), Modelling streamwater chemistry as a mixture of soilwater end-members—An application to the Panola Mountain catchment, Georgia, U.S.A., *J. Hydrol.*, *116*(1–4), 321–343.
House, W. A., and M. S. Warwick (1998), Hysteresis of the solute concentration/discharge relationship in rivers during storms, *Water Res.*, *32*(8), 2279–2290.
Jacques, D., J. Šimůnek, D. Mallants, and M. T. van Genuchten (2006), Operator-splitting errors in coupled reactive transport codes for transient variably saturated flow and contaminant transport in layered soil profiles, *J. Contam. Hydrol.*, *88*(3), 197–218.
James, L. D. (1972), Hydrologic modeling, parameter estimation, and watershed characteristics, *J. Hydrol.*, *17*(4), 283–307.
Jarboe, J. E., and C. Haan (1974), Calibrating a water yield model for small ungaged watersheds, *Water Resour. Res.*, *10*(2), 256–262.
Jin, L., and S. L. Brantley (2011), Soil chemistry and shale weathering on a hillslope influenced by convergent hydrologic flow regime at the Susquehanna/Shale Hills Critical Zone Observatory, *Appl. Geochem.*, *26,suppl.0*, S51–S56.
Jin, L., R. Ravella, B. Ketchum, P. R. Bierman, P. Heaney, T. White, and S. L. Brantley (2010), Mineral weathering and elemental transport during hillslope evolution at the Susquehanna/Shale Hills Critical Zone Observatory, *Geochim. Cosmochim. Acta*, *74*(13), 3669–3691.
Jin, L., D. M. Andrews, G. H. Holmes, H. Lin, and S. L. Brantley (2011), Opening the "Black Box": Water chemistry reveals hydrological controls on weathering in the Susquehanna Shale Hills Critical Zone Observatory, *Vadose Zone J.*, *10*(3), 928–942.
Jin, L., N. Ogrinc, T. Yesavage, E. A. Hasenmueller, L. Ma, P. L. Sullivan, J. Kaye, C. Duffy, and S. L. Brantley (2014), The CO_2 consumption potential during gray shale weathering: Insights from the evolution of carbon isotopes in the Susquehanna Shale Hills Critical Zone Observatory, *Geochim. Cosmochim. Acta*, *142*, 260–280.
Johnson, N. M., G. E. Likens, F. H. Bormann, D. W. Fisher, and R. S. Pierce (1969), A working model for the variation in stream water chemistry at the Hubbard Brook Experimental Forest, New Hampshire, *Water Resour. Res.*, *5*(6), 1353–1363.
Kang, Q. J., P. C. Lichtner, and D. X. Zhang (2006), Lattice Boltzmann pore-scale model for multicomponent reactive transport in porous media, *J. Geophys. Res.*, *111*, B05203, doi:10.1029/2005JB003951.
Kirchner, J. W. (2003), A Double Paradox in catchment hydrology and geochemistry, *Hydrol. Processes*, *17*(4), 871–874.
Kirchner, J. W., and C. Neal (2013), Universal fractal scaling in stream chemistry and its implications for solute transport and water quality trend detection, *Proc. Natl. Acad. Sci. U. S. A.*, *110*, 12,213–12,218.
Köhler, S. J., F. Dufaud, and E. H. Oelkers (2003), An experimental study of illite dissolution kinetics as a function of pH from 1.4 to 12.4 and temperature from 5 to 50°C, *Geochim. Cosmochim. Acta*, *67*(19), 3583–3594.
Köhler, S. J., D. Bosbach, and E. H. Oelkers (2005), Do clay mineral dissolution rates reach steady state?, *Geochim. Cosmochim. Acta*, *69*(8), 1997–2006.
Krumins, V., M. Gehlen, S. Arndt, P. Van Cappellen, and P. Regnier (2013), Dissolved inorganic carbon and alkalinity fluxes from coastal marine sediments: Model estimates for different shelf environments and sensitivity to global change, *Biogeosciences*, *10*(1), 371–398.
Kumar, M., C. J. Duffy, and K. M. Salvage (2009), A second-order accurate, Finite Volume-Based, Integrated Hydrologic Modeling (FIHM) framework for simulation of surface and subsurface flow, *Vadose Zone J.*, *8*(4), 873–890.
Kump, L. R., S. L. Brantley, and M. A. Arthur (2000), Chemical weathering, atmospheric CO_2, and climate, *Annu. Rev. Earth Planet Sci.*, *28*, 611–667.
Lasaga, A. (1981), *Kinetics of Geochemical Processes*, 169 pp.
Lasaga, A. C. (1984), Chemical kinetics of water-rock interactions, *J. Geophys. Res.*, *89*(B6), 4009–4025.
Li, L., C. I. Steefel, and L. Yang (2008), Scale dependence of mineral dissolution rates within single pores and fractures, *Geochim. Cosmochim. Acta*, *72*(2), 360–377.
Li, L., C. I. Steefel, M. B. Kowalsky, A. Englert, and S. S. Hubbard (2010), Effects of physical and geochemical heterogeneities on mineral transformation and biomass accumulation during biostimulation experiments at Rifle, Colorado, *J. Contam. Hydrol.*, *112*(1–4), 45–63.
Li, L., et al. (2017a), Expanding the role of reactive transport models in critical zone processes, *Earth Sci. Rev.*, *165*, 280–301.
Li, L., C. Bao, P. Sullivan, S. Brantley, Y. Shi, and C. Duffy (2017b), Understanding Watershed Hydrogeochemistry: 2. Synchronized hydrological and geochemical processes drive stream chemostatic behavior, *Water Resour. Res.*, *53*, doi:10.1002/2016WR018935.
Li, S., and C. J. Duffy (2012), Fully-coupled modeling of shallow water flow and pollutant transport on unstructured grids, *Procedia Environ. Sci.*, *13*, 2098–2121.
Lichtner, P. C. (1985), Continuum model for simultaneous chemical-reactions and mass-transport in hydrothermal systems, *Geochim. Cosmochim. Acta*, *49*(3), 779–800.
Lichtner, P. C. (1988), The quasi-stationary state approximation to coupled mass-transport and fluid-rock interaction in a porous-medium, *Geochim. Cosmochim. Acta*, *52*(1), 143–165.
Lichtner, P. C. (1996), Continuum formulation of multicomponent-multiphase reactive transport, in *Reactive Transport in Porous Media*, edited by P. C. Lichtner, C. I. Steefel, and E. H. Oelkers, pp. 1–81, Mineral. Soc. of Am., Washington, D. C.
Lichtner, P. C., C. I. Steefel, E. H. Oelkers, U. P. Sabatier, D. Suarez, and J. Simdnek (1996), Reactive transport in porous media.

Lin, H. (2006), Temporal stability of soil moisture spatial pattern and subsurface preferential flow pathways in the Shale Hills Catchment, *Vadose Zone J.*, *5*(1), 317–340.
Liu, C., J. M. Zachara, N. P. Qafoku, and Z. Wang (2008), Scale-dependent desorption of uranium from contaminated subsurface sediments, *Water Resour. Res.*, *44*, W08413, doi:10.1029/2007WR006478.
Liu, C., J. Shang, H. Shan, and J. M. Zachara (2013), Effect of subgrid heterogeneity on scaling geochemical and biogeochemical reactions: A case of U(VI) desorption, *Environ. Sci. Technol.*, *48*(3), 1745–1752.
MacQuarrie, K. T. B., and K. U. Mayer (2005), Reactive transport modeling in fractured rock: A state-of-the-science review, *Earth Sci. Rev.*, *72*(3–4), 189–227.
Maher, K., C. I. Steefel, A. F. White, and D. A. Stonestrom (2009), The role of reaction affinity and secondary minerals in regulating chemical weathering rates at the Santa Cruz Soil Chronosequence, California, *Geochim. Cosmochim. Acta*, *73*, 2804–2831.
Maxwell, R. M., and N. L. Miller (2005), Development of a coupled land surface and groundwater model, *J. Hydrometeorol.*, *6*(3), 233–247.
Mayer, K. U., S. G. Benner, E. O. Frind, S. F. Thornton, and D. N. Lerner (2001), Reactive transport modeling of processes controlling the distribution and natural attenuation of phenolic compounds in a deep sandstone aquifer, *J. Contam. Hydrol.*, *53*(3–4), 341–368.
Mayer, K. U., E. O. Frind, and D. W. Blowes (2002), Multicomponent reactive transport modeling in variably saturated porous media using a generalized formulation for kinetically controlled reactions, *Water Resour. Res.*, *38*(9), 1174, doi:10.1029/2001WR000862.
McDonnell, J., M. Sivapalan, K. Vaché, S. Dunn, G. Grant, R. Haggerty, C. Hinz, R. Hooper, J. Kirchner, and M. Roderick (2007), Moving beyond heterogeneity and process complexity: A new vision for watershed hydrology, *Water Resour. Res.*, *43*, W07301, doi:10.1029/2006WR005467.
McGlynn, B. L., and J. J. McDonnell (2003), Role of discrete landscape units in controlling catchment dissolved organic carbon dynamics, *Water Resour. Res.*, *39*(4), 1090, doi:10.1029/2002WR001525.
McGuire, K. J., and J. J. McDonnell (2010), Hydrological connectivity of hillslopes and streams: Characteristic time scales and nonlinearities, *Water Resour. Res.*, *46*, W10543, doi:10.1029/2010WR009341.
Molins, S., D. Trebotich, L. Yang, J. B. Ajo-Franklin, T. J. Ligocki, C. Shen, and C. I. Steefel (2014), Pore-scale controls on calcite dissolution rates from flow-through laboratory and numerical experiments, *Environ. Sci. Technol.*, *48*(13), 7453–7460.
Montanari, A., J. Bahr, G. Blöschl, X. Cai, D. S. Mackay, A. M. Michalak, H. Rajaram, and G. Sander (2015), Fifty years of *Water Resources Research*: Legacy and perspectives for the science of hydrology, *Water Resour. Res.*, *51*, 6797–6803, doi:10.1002/2015WR017998.
Moore, J., P. C. Lichtner, A. F. White, and S. L. Brantley (2012), Using a reactive transport model to elucidate differences between laboratory and field dissolution rates in regolith, *Geochim. Cosmochim. Acta*, *93*, 235–261.
Navarre-Sitchler, A., and S. Brantley (2007), Basalt weathering across scales, *Earth Planet. Sci. Lett.*, *261*, 321–334.
Navarre-Sitchler, A. K., R. M. Maxwell, E. R. Siirila, G. E. Hammond, and P. C. Lichtner (2013), Elucidating geochemical response of shallow heterogeneous aquifers to CO_2 leakage using high-performance computing: Implications for monitoring of CO_2 sequestration, *Adv. Water Resour.*, *53*, 45–55.
Neuman, S. P., L. Xue, M. Ye, and D. Lu (2012), Bayesian analysis of data-worth considering model and parameter uncertainties, *Adv. Water Resour.*, *36*, 75–85.
Ortoleva, P., E. Merino, C. Moore, and J. Chadam (1987), Geochemical self-organization, I. Feedbacks, quantitative modeling, *Am. J. Sci.*, *287*, 979–1007.
Perrochet, P., and D. Bérod (1993), Stability of the standard Crank-Nicolson-Galerkin Scheme applied to the diffusion-convection equation: Some new insights, *Water Resour. Res.*, *29*(9), 3291–3297.
Pokhrel, P., and H. V. Gupta (2010), On the use of spatial regularization strategies to improve calibration of distributed watershed models, *Water Resour. Res.*, *46*, W01505, doi:10.1029/2009WR008066.
Prommer, H., D. A. Barry, and C. Zheng (2003), MODFLOW/MT3DMS-based reactive multi-component transport modeling, *Ground Water*, *41*(2), 247–257.
Qiao, C., L. Li, R. T. Johns, and J. Xu (2015), Compositional modeling of dissolution-induced injectivity alteration during CO_2 flooding in carbonate reservoirs, *SPE J.*, *21*.
Qu, Y., and C. J. Duffy (2007), A semidiscrete finite volume formulation for multiprocess watershed simulation, *Water Resour. Res.*, *43*, W08419, doi:10.1029/2006WR005752.
Quinn, P., K. Beven, P. Chevallier, and O. Planchon (1991), The prediction of hillslope flow paths for distributed hydrological modelling using digital terrain models, *Hydrol. Processes*, *5*(1), 59–79.
Refsgaard, J. C., and B. Storm (1995), MIKE SHE, in *Computer Models of Watershed Hydrology*, edited by V. P. Singh, pp. 809–846, Water Resour. Publ.
Regnier, P., R. Wollast, and C. I. Steefel (1997), Long-term fluxes of reactive species in macrotidal estuaries: Estimates from a fully transient, multicomponent reaction-transport model, *Mar. Chem.*, *58*(1–2), 127–145.
Roelandt, C., Y. Goddéris, M. P. Bonnet, and F. Sondag (2010), Coupled modeling of biospheric and chemical weathering processes at the continental scale, *Global Biogeochem. Cycles*, *24*, GB2004, doi:10.1029/2008GB003420.
Salehikhoo, F., and L. Li (2015), The role of magnesite spatial distribution patterns in determining dissolution rates: When do they matter?, *Geochim. Cosmochim. Acta*, *155*, 107–121.
Santhi, C., J. G. Arnold, J. R. Williams, W. A. Dugas, R. Srinivasan, and L. M. Hauck (2001), VALIDATION OF THE SWAT MODEL ON A LARGE RWER BASIN WITH POINT AND NONPOINT SOURCES, *J. Am. Water Resour. Assoc.*, *37*, 1169–1188.
Saunders, J. A., and L. E. Toran (1995), Modeling of radionuclide and heavy metal sorption around low- and high-{pH} waste disposal sites at {Oak Ridge, Tennessee}, *Appl. Geochem.*, *10*(6), 673–684.
Scheibe, T. D., E. M. Murphy, X. Chen, A. K. Rice, K. C. Carroll, B. J. Palmer, A. M. Tartakovsky, I. Battiato, and B. D. Wood (2015), An analysis platform for multiscale hydrogeologic modeling with emphasis on hybrid multiscale methods, *Ground Water*, *53*(1), 38–56.
Shen, C., and M. S. Phanikumar (2010), A process-based, distributed hydrologic model based on a large-scale method for surface–subsurface coupling, *Adv. Water Resour.*, *33*(12), 1524–1541.
Shi, Y., K. J. Davis, C. J. Duffy, and X. Yu (2013), Development of a coupled land surface hydrologic model and evaluation at a Critical Zone Observatory, *J. Hydrometeorol.*, *14*(5), 1401–1420.
Singh, V. P. (1995), *Computer Models of Watershed Hydrology*, Water Resour. Publ.
Soler, J. M., and U. K. Mader (2005), Interaction between hyperalkaline fluids and rocks hosting repositories for radioactive waste: Reactive transport simulations, *Nucl. Sci. Eng.*, *151*(1), 128–133.
Song, X., J. Zhang, C. Zhan, Y. Xuan, M. Ye, and C. Xu (2015), Global sensitivity analysis in hydrological modeling: Review of concepts, methods, theoretical framework, and applications, *J. Hydrol.*, *523*, 739–757.

Steefel, C. I., and A. C. Lasaga (1994), A coupled model for transport of multiple chemical species and kinetic precipitation/dissolution reactions with application to reactive flow in single phase hydrothermal systems, *Am. J. Sci.*, *294*(5), 529–592.
Steefel, C. I., D. J. DePaolo, and P. C. Lichtner (2005), Reactive transport modeling: An essential tool and a new research approach for the Earth Sciences, *Earth Planet. Sci. Lett.*, *240*, 539–558.
Steefel, C. I., et al. (2014), Reactive transport codes for subsurface environmental simulation, *Comput. Geosci.*, *19*(3), 445–478.
Steefel, C. I., et al. (2015), Reactive transport codes for subsurface environmental simulation, *Comput. Geosci.*, *19*(3), 445–478.
Therrien, R., R. McLaren, E. Sudicky, and S. Panday (2010), *HydroGeoSphere: A Three-Dimensional Numerical Model Describing Fully-Integrated Subsurface and Surface Flow and Solute Transport*, Groundwater Simul. Group, Univ. of Waterloo, Waterloo, Ont., Canada.
Toler, L. (1965), Relation between chemical quality and water discharge in Spring Creek, southwestern Georgia, *U.S. Geol. Surv. Prof. Pap.*, *525*, C209–C213.
Torres, M. A., A. J. West, and K. E. Clark (2015), Geomorphic regime modulates hydrologic control of chemical weathering in the Andes–Amazon, *Geochim. Cosmochim. Acta*, *166*, 105–128.
Van Cappellen, P., and Y. F. Wang (1996), Cycling of iron and manganese in surface sediments: A general theory for the coupled transport and reaction of carbon, oxygen, nitrogen, sulfur, iron, and manganese, *Am. J. Sci.*, *296*, 197–243.
Van Genuchten, M. T. (1980), A closed-form equation for predicting the hydraulic conductivity of unsaturated soils, *Soil Sci. Soc. Am. J.*, *44*(5), 892–898.
VanderKwaak, J. E., and K. Loague (2001), Hydrologic-response simulations for the R-5 catchment with a comprehensive physics-based model, *Water Resour. Res.*, *37*(4), 999–1013.
Vanselow, A. P. (1932), Equilibria of the base-exchange reactions of bentonites, permutites, soil colloids, and zeolites, *Soil Sci.*, *33*(2), 95–114.
Walsh, M., S. Bryant, R. Schechter, and L. Lake (1984), Precipitation and dissolution of solids attending flow through porous media, *AIChE J.*, *30*(2), 317–328.
White, A. F. (1995), Chemical weathering rates of silicate minerals in soils, in *Chemical Weathering Rates of Silicate Minerals*, edited by A. F. White and S. L. Brantley, pp. 407–461, Mineral. Soc. of Am., Washington, D. C.
White, A. F., and S. L. Brantley (2003), The effect of time on the weathering of silicate minerals: why do weathering rates differ in the laboratory and field?, *Chem. Geol.*, *202*(3–4), 479–506.
White, M. D., and M. Oostrom (2000), STOMP: Subsurface Transport Over Multiple Phases (Version 2.0): Theory Guide, Richland, WA.
Wolery, T. J. (1992), *EQ3/6: A Software Package for Geochemical Modeling of Aqueous Systems: Package Overview and Installation Guide (Version 7.0)*, Lawrence Livermore Natl. Lab., Livermore, Calif.
Xia, Y., K. Mitchell, M. Ek, J. Sheffield, B. Cosgrove, E. Wood, L. Luo, C. Alonge, H. Wei, and J. Meng (2012), Continental-scale water and energy flux analysis and validation for the North American Land Data Assimilation System project phase 2 (NLDAS-2): 1. Intercomparison and application of model products, *J. Geophys. Res.*, *117*, D03109, doi:10.1029/2011JD016048.
Xu, T., J. Samper, C. Ayora, M. Manzano, and E. Custodio (1999), Modeling of non-isothermal multi-component reactive transport in field scale porous media flow systems, *J. Hydrol.*, *214*(1–4), 144–164.
Xu, T. F., J. A. Apps, and K. Pruess (2003), Reactive geochemical transport simulation to study mineral trapping for CO_2 disposal in deep arenaceous formations, *J. Geophys. Res.*, *108*(B2), 2071, doi:10.1029/2002JB001979.
Xu, T., E. Sonnenthal, N. Spycher, and K. Pruess (2006), TOUGHREACT—A simulation program for non-isothermal multiphase reactive geochemical transport in variably saturated geologic media: Applications to geothermal injectivity and CO_2 geological sequestration, *Comput. Geosci.*, *32*(2), 145–165.
Yabusaki, S. B., Y. Fang, K. H. Williams, C. J. Murray, A. L. Ward, R. D. Dayvault, S. R. Waichler, D. R. Newcomer, F. A. Spane, and P. E. Long (2011), Variably saturated flow and multicomponent biogeochemical reactive transport modeling of a uranium bioremediation field experiment, *J. Contam. Hydrol.*, *126*(3–4), 271–290.
Ye, M., P. D. Meyer, and S. P. Neuman (2008), On model selection criteria in multimodel analysis, *Water Resour. Res.*, *44*, W03428, doi:10.1029/2008WR006803.
Yeh, G.-T., G. Huang, H.-p. Cheng, F. Zhang, H.-c. Lin, E. Edris, and D. Richards (2006), A first principle, physics based watershed model: WASH123D, in *Watershed Models*, edited by V. P. Singh and D. K. Frevert, CRC Press, Boca Raton, Fla.
Yeh, G. T., and V. S. Tripathi (1989), A critical evaluation of recent developments in hydrogeochemical transport models of reactive multichemical components, *Water Resour. Res.*, *25*(1), 93–108.
Zhang, L., D. A. Dzombak, D. V. Nakles, J.-P.L. Brunet, and L. Li (2013), Reactive transport modeling of interactions between acid gas ($CO_2 + H_2S$) and pozzolan-amended wellbore cement under geologic carbon sequestration conditions, *Energy Fuels*, *27*(11), 6921–6937.
Zhang, Y., R. Slingerland, and C. Duffy (2016), Fully-coupled hydrologic processes for modeling landscape evolution, *Environ. Modell. Software*, *82*, 89–107.
Zhu, Y., L. Shi, L. Lin, J. Yang, and M. Ye (2012), A fully coupled numerical modeling for regional unsaturated–saturated water flow, *J. Hydrol.*, *475*, 188–203.
Zysset, A., F. Stauffer, and T. Dracos (1994), Modeling of chemically reactive groundwater transport, *Water Resour. Res.*, *30*(7), 2217–2228.